points. After these points are identified, the DGHT algorithm is applied.

4.3.1. The dynamic generalized Hough transform algorithm

The Hough transform decomposes a boundary into its constituent shape primitives. In principle, for any analytically given curve, the DGHT can be used to compute all of the parameters associated with the curve (Leavers 1992). In the present case, we will apply the DGHT algorithm for detection of the ellipsoidal shape, since it was already assumed that the bubble would have an ellipsoidal shape according to the values of the parameters Re, Eo and M. In this analysis, the equation for an ellipse is written as (Leavers 1992)

$$x^2 + y^2 - A\left(x^2 - y^2\right) - 2Bxy - Cx - Dy - E = 0. \qquad [12]$$

Randomly choosing five of the connectivity points, one can solve for A, B, C, D, and E, by utilizing, for example, Gauss elimination with back propagation. The ellipse parameters are estimated after each iteration. The five parameters A, B, C, D, and E, are related to the ellipse parameters through

$$\theta = \frac{1}{2}\arctan\left(\frac{B}{A}\right) \qquad [13]$$

$$e = \sqrt{\frac{\cos 2\theta - A}{\cos 2\theta + A}} \qquad [14]$$

$$y_0 = \frac{1}{2}\frac{D(1-A) + BC}{1 - A^2 - B^2} \qquad [15]$$

$$x_0 = \frac{1}{2}\frac{C + 2\,y_0\,B}{1 - A} \qquad [16]$$

$$a = \sqrt{\frac{\left(1+e^2\right)\left(E + x_0\frac{C}{2} + y_0\frac{D}{2}\right)}{2e^2}} \qquad [17]$$

$$b = a\,e \qquad [18]$$

where θ is the rotation angle of the ellipse from the horizontal axis; e is the eccentricity (the ratio of the semiminor to semimajor axis); x_0 and y_0 are the center coordinates of the ellipse; a is the semiaxis in the X-direction; and b is the semiaxis in the Y-direction.

Although effective stopping criteria to end the calculation cycle for the DGHT algorithm is known, here it was simply iterated for a number of times. For the case of images from the PIV cameras, 150000 iterations were performed, while 10000 iterations were performed for the images from the shadow camera. These numbers for the iteration process were chosen by considering the average number of the connectivity points available, as well as the quality of such points. It should be mentioned that between 30 and 50% of the iterations for the PIV images did not yield values that satisfied the ellipse equation [12]. The shadow images successfully satisfied equation [12] about 90% of the iterations. For each parameter, the value with the highest frequency corresponds to the value that best satisfies the ellipse equation.

4.3.2. Accuracy of the reconstruction

After the iteration process finishes, the computed parameters of the ellipse can be used to draw the ellipse that best fits the connectivity points employed in the DGHT algorithm. Figures 10e and 11e show the ellipse that best satisfied the connectivity points given in figures 10d and 11d, respectively. Once the ellipse parameters are known, one can visually overlay the reconstructed ellipse over the original image for a fast comparison of the reconstruction process accuracy. Figures 10f and 11f present an overlay of the reconstructed ellipse and the original images 9a and 9b. The results are very encouraging; the agreement between the reconstructed ellipse and the original image is very good even for the PIV image. These images demonstrated the capabilities of the DGHT to be used in the study of bubbly flow images.

Histograms can be constructed for each parameter. The width of the histogram is related to the standard deviation, so it is a direct measurement of the uncertainty associated with the determined parameter. A well-defined, isolated peak indicates that the parameter has a good statistical value. When the distribution (the histogram) shows multiple or wide peaks, the quantity or quality of the connectivity points is insufficient or bad. Histograms of θ, x_0 and a are showed in figures 12 and 13, for the PIV and shadow images analyzed here, respectively. Clearly, the shadow image produced narrow and sharp peaks for x_0 and a; while these

(a)

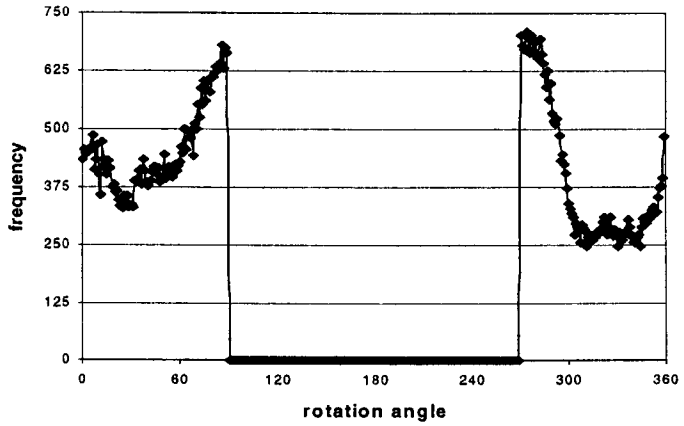

(b)

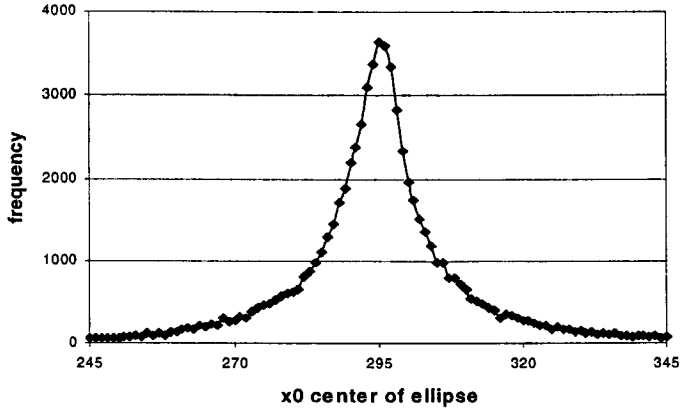

(c)

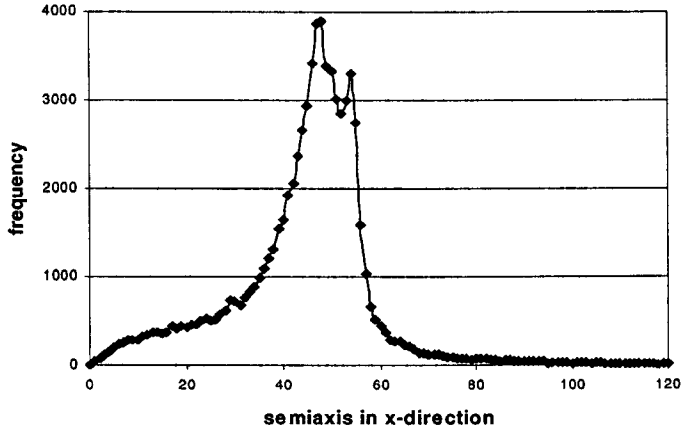

Figure 12. Histograms of three of the parameters of the ellipse that best fits the bubble in figure 9a, computed through the DGHT. a) Rotation angle; b) center of the ellipse on the x-direction; and c) value of the semiaxis on the x-direction.

(a)

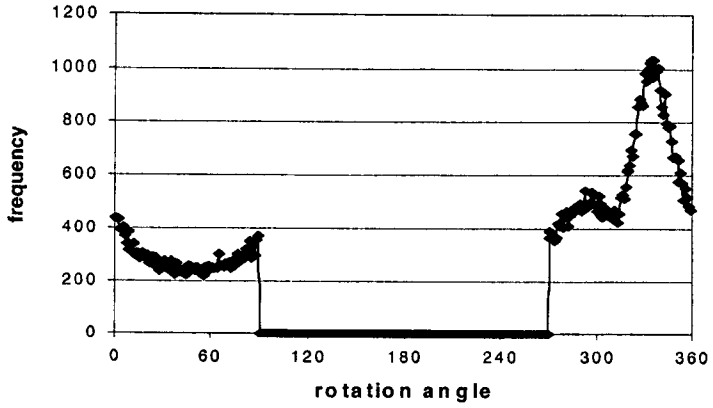

(b)

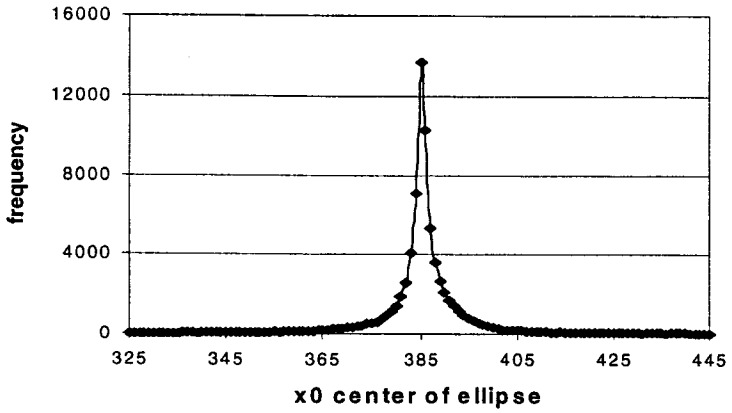

(c)

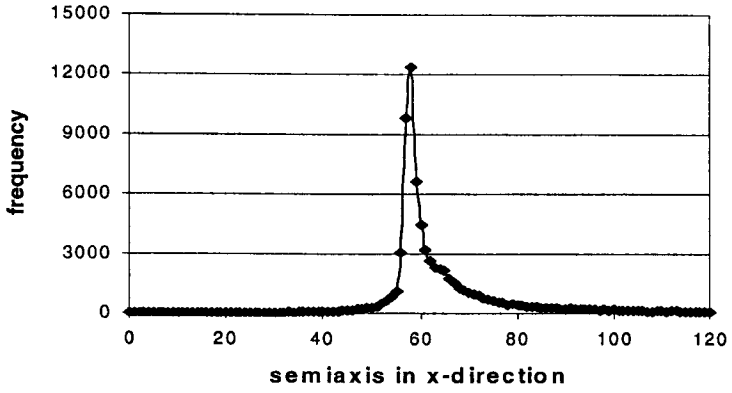

Figure 13. Histograms of three of the parameters of the ellipse that best fits the bubble in figure 9b, computed through the DGHT. a) Rotation angle; b) center of the ellipse on the x-direction; and c) value of the semiaxis on the x-direction.

parameters from the PIV image show wider and bimodal peaks, as a consequence of the quality of the connectivity points used. For the PIV image, it should be mentioned that in the Y-direction the parameters produced well-defined peaks, because more information was available in the direction.

With respect to the rotation angle, both images yielded small and wide peaks. This, however, is not a failure of the DGHT, but a consequence of the very close values of the semiaxes. In other words, when a and b are close to each other, the ellipse becomes closer to a circle, and therefore the rotation angle becomes more undefined.

The DGHT algorithm offers some advantages over other reconstruction techniques. It yields all five parameters associated with the bubble, so dimensions, shape and travel path can be determined. Other techniques, simply interpolate, and sometimes extrapolate, between the boundary points available for the reconstruction. Although this can give a closer match to the real shape of the bubble, the dimensions and 3D movement will have to be determined by other means. Memory storage and computation time in the DGHT algorithm are low. When occlusion of objects exists the DGHT algorithm has also been proven to get good results. The primary disadvantage of this scheme is the need for an *a priori* analytical expression for the curve to be detected. Thus, for a very distorted bubble, the best that the DGHT algorithm can achieve is the approximation of the actual shape to a given curve.

4.4. Three-dimensional bubble shape reconstruction

Once the parameters of the ellipse are known for both the PIV and the shadow images, it is necessary to compute these parameters in world coordinates. Observe that the world coordinates can be easily calculated in this case, because the PIV center and the shadow cameras are parallel to the XZ and YZ planes, respectively, as demonstrated in Chapter II. The process is very similar process to that of the 3D reconstruction of the position of the tracer particles, shown in Chapter III. The calibration curves for calculating world coordinates from image coordinates are shown in figure 14.

After combining the parameters of ellipses from each view, a 3D reconstruction was achieved. The parameters of this bubble were the following. The centroid of the bubble was located at X_0 = -0.16 mm, Y_0 = -1.99 mm, and Z_0 = 3.86 mm. The values of the semiaxes were: on the X-direction, a = 1.24 mm; on the Y-direction, b = 1.46 mm; and on the Z-direction, c = 1.39 mm. The rotation angles about the Y and the X axes were α = -4 and β = 25 degrees,

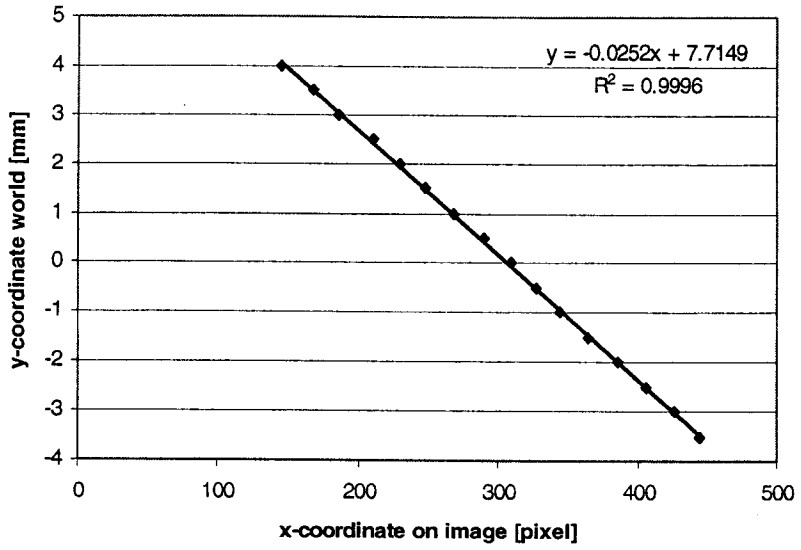

(a)

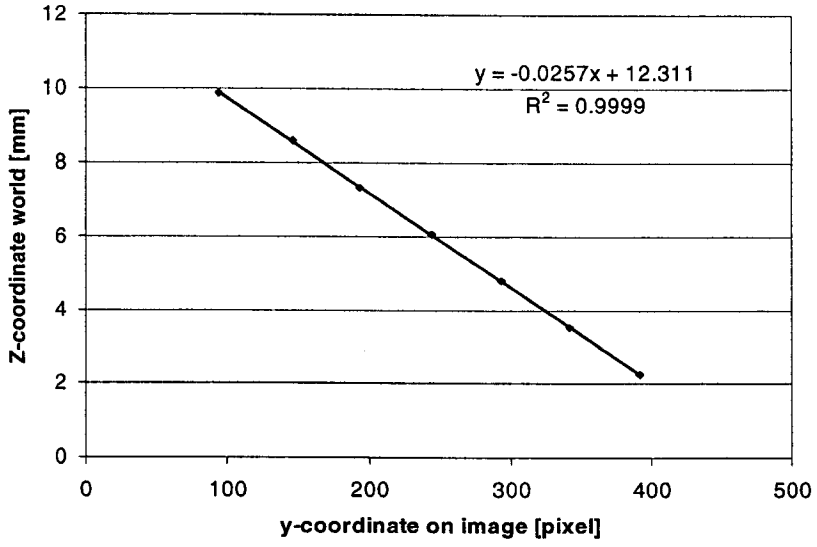

(b)

Figure 14. Calibration curves for computing world coordinates from image coordinates. a) Variation of y against u on images from the Shadow camera; and b) variation of z against v for images from both the Shadow and the Center cameras.

respectively. These angles are measured positive from the z-axis, and are positive counter-clockwise. The spherical-equivalent radius of the bubble was 1.36 mm. The scale factors used for the calculations were 38.8 pixel/mm, 39.7 pixel/mm, and 39.5 pixel/mm on the X-, Y-, and Z-directions, respectively.

Figures 15 presents three different views of the 3D reconstructed bubble. Experimental data for air bubbles rising in stagnant water indicate that for a bubble with a spherical-equivalent radius of the computed dimensions, the shape of the bubble should be very close to an sphere. Observe that the bubble reconstructed here is very close to a spheroid.

Finally, the error associated with the reconstruction algorithm presented was always less than 3 pixel (0.08 mm). This maximum error is obviously for the PIV image, on the X-direction. For the localization of the centroid the error is smaller, but it will be considered as 3 pixel in the error analysis calculations.

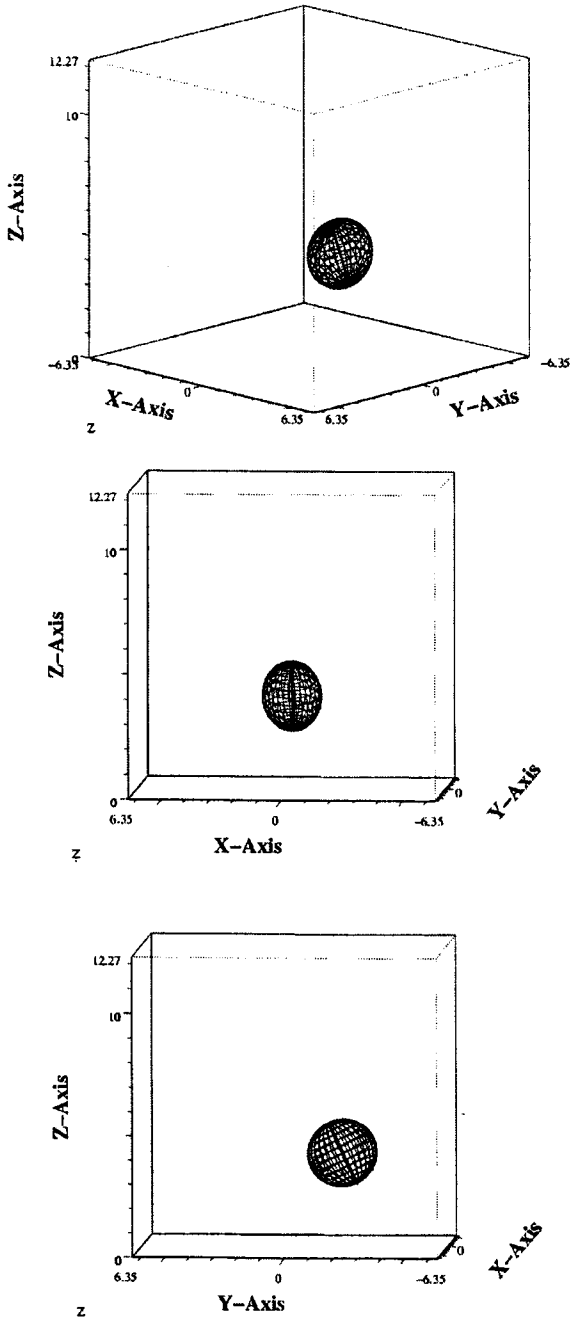

Figure 15. Three different views of the three-dimensional reconstruction of the bubble shown in figure 9, after combining information from the two-dimensional reconstructions shown in figures 10e and 11e.

CHAPTER V
FLOW AROUND A RISING BUBBLE AND WITHIN ITS WAKE

The previous chapters have dealt with the development of a methodology capable of providing transient, three-dimensional information about the flow field generated by a freely rising bubble in a liquid. Such methodology is based on the measurement capabilities of the PIV technique. Furthermore, with the aid of the SPIV technique, an accurate quantitative and qualitative description of the bubble shape fluctuation, orientation, and trajectory can be obtained. In this chapter, the experimental results concerning the flow field upstream and downstream of an ellipsoidal air bubble rising in stagnant water, in a small-diameter pipe are presented and discussed. The wall influence on the development and behavior of the liquid flow is particularly addressed. The information obtained from the SPIV measurements is presented in the next chapter.

This chapter first presents an analysis of the uncertainties associated to the PIV measurements, and then the error propagation in the calculations of average and fluctuating quantities, vorticity, and kinetic energy. Then a brief theoretical background of the flow around bubbles is presented. Finally, the experimental data is presented and discussed.

5.1. Uncertainty analysis of PIV measurements and error propagation

Flow visualization techniques cannot resolve the whole time and length scales due to camera resolution and limited frame rate. In our measurements, limits on the minimum and maximum range of the 2D tracks were set after analyzing many of the acquired pictures. It was found that 4 pixels $\leq u \leq$ 25 pixels (38.80 pixels/mm), and 4 pixels $\leq v \leq$ 40 pixels (19.56 pixels/mm) were the optimum values for the 2D tracking of the velocity vectors. In terms of the velocity units, the ranges are 6.19 mm/s $\leq V_u \leq$ 38.66 mm/s, and 12.27 mm/s $\leq V_v \leq$ 122.72 mm/s.

The uncertainty in the velocity measurements is a direct consequence of a combination of errors from three main sources. These are the localization of the centroid of the seed particle images and their displacements in the 2D images, the determination of the 3D position of the seed particles, and the uncertainty of how well the tracer particles follow the actual fluid motion. These uncertainties are considered in detail next.

5.1.1. The Stokes number

Estimation of how closely the seed particles follow the flow, or how fast the seed particles respond to the flow changes, can be calculated utilizing the particle Stokes number. This parameter can be calculated as the ratio of the relaxation time of the seed particle to the characteristic time of the flow. The particle relaxation time, τ_p, also known as the momentum or velocity response time, is the time needed by a seed particle to reach $e^{-1}U$, if the particle was initially at rest. Here U is the fluid velocity. The time τ_p can be computed from

$$\tau_p = \frac{(2\rho_p + \rho_f)\, d_p^2}{36\,\mu_f}, \qquad [19]$$

where ρ is the density, d the seed tracer diameter, μ the viscosity, and the subscript p refers to particle properties, and f to the fluid properties. In this experiment, the relaxation time of the seed was calculated to be 140 μs. The fluid time scale, τ_f, is the time needed by the fluid to be advected a characteristic length L, that is,

$$\tau_f = \frac{L}{U}. \qquad [20]$$

For the characteristic time of the flow, an equivalent diameter of the bubble of 3 mm was used as the characteristic length, and the maximum measurable liquid velocity. The resultant time was 24 ms. Then, the Stokes number, τ_p/τ_f, was calculated to be 5.72×10^{-3}. Therefore the 40 μm seed particles closely followed the fluid motion changes, and therefore did not significantly contribute to the total error.

5.1.2. Accuracy of two-dimensional localization of particle centroid

Adrian (1986) determined the error associated in localizing the 2D particle-image centroids, and their displacements between two or more consecutive frames. For the continuous laser employed in this experiment, the uncertainty in the time interval comes from the laser pulse width, (250 μs), so it had a negligible effect on the total error of the velocity measurements. The error in locating the centroid displacements depends on the optical parameters of the camera,

lenses, and laser, and the algorithm for finding the particle-image centroid. The FINDSPOTS computer program (Blanchat 1992) used has a subpixel accuracy of about 95%, and the magnification of the system used in the experiment allowed for even better accuracy. The error in determining the centroid displacement was less than 1% of the total error.

5.1.3. Uncertainty of three-dimensional particle position and instantaneous velocity

The main error source in the velocity measurements was the calculation of the three world coordinates of the seed particles. For this type of error, the calibration is the main source, since it was done by using a least squares method, as explained in Chapter II. To calculate the error associated with each world coordinate, [11] was used to compute the 3D positions of all the calibration points. Then, the computed values were compared against the known positions of the calibration points. The root mean square (r.m.s.) error in each direction σ_x, σ_y, and σ_z, respectively, was 26.4 μm in the X-direction; 96.1 μm in the Y-direction; and 23.2 μm in the Z-direction. In terms of the velocity, the r.m.s. error for each component, σ_u, σ_v, and σ_w, respectively, was: 1.58 mm/s in the x-component; 5.77 mm/s in the y-component; and 1.39 mm/s in the z-component. These values are estimated for a framing rate of 60 Hz. It can be concluded that the error associated with small magnitude velocity vectors can be significant.

5.1.4. Error propagation

If the errors associated to a measurement are small and symmetric around zero, the standard deviation for any quantity s, σ_s, derived from, say, three measurements is given by

$$\sigma_s^2 = \left(\frac{\partial s}{\partial r_1}\right)^2 \sigma_{r1}^2 + \left(\frac{\partial s}{\partial r_2}\right)^2 \sigma_{r2}^2 + \left(\frac{\partial s}{\partial r_3}\right)^2 \sigma_{r3}^2, \qquad [21]$$

where r_1, r_2, and r_3 are the values of the measurements, and σ_{r1}, σ_{r2}, and σ_{r3}, are their respective associated errors. This equation is known as the *error propagation formula*, and it will be used for the calculations of the errors of the quantities derived from the velocity measurements and their associated errors.

For the calculation of the velocity gradients, the central finite difference scheme, given by

$$\frac{\partial u_i}{\partial r} \approx \frac{u_{i+1} - u_{i-1}}{2\Delta r}, \qquad [22]$$

which has a second order accuracy, was used. The error for the gradient of the u velocity component, for example, can be computed by observing that the function s, in this case, is an addition of measurements, so using [21],

$$\sigma_{ur} = \sqrt{\left(\sigma_u^2 + \sigma_u^2\right)}, \qquad [23]$$

where it has been assumed that the σ_u is the same at every point. Then, $\sigma_{ur} = 2.23$ Hz. For the rest of the components, $\sigma_{vr} = 8.16$ Hz, and $\sigma_{wr} = 1.97$ Hz.

The vorticity vector is given by

$$\boldsymbol{\omega} = \left(\frac{\partial w}{\partial y} - \frac{\partial v}{\partial z}\right)\mathbf{i} + \left(\frac{\partial u}{\partial z} - \frac{\partial w}{\partial x}\right)\mathbf{j} + \left(\frac{\partial v}{\partial x} - \frac{\partial u}{\partial y}\right)\mathbf{k}. \qquad [24]$$

Thus, the error for the vorticity vector components was estimated through equations similar to [23], that is,

$$\sigma_{\omega x} = \sqrt{\left(\sigma_{wy}^2 + \sigma_{vz}^2\right)}. \qquad [25]$$

Therefore $\sigma_{\omega x} = 8.39$ Hz, $\sigma_{\omega y} = 8.16$ Hz, and $\sigma_{\omega z} = 1.97$ Hz.

For the calculation of the error in the average [21] yields, for the $\overline{u}$ velocity component, as an example,

$$\sigma_{\overline{u}} = \frac{\sigma_u}{\sqrt{n}}, \qquad [26]$$

where n is the number of samples utilized in the average operation. The expressions for $\overline{v}$ and $\overline{w}$ are similar. The error associated to the mean kinetic energy,

$$\overline{\mathrm{K}} = \frac{1}{2} m\left(\overline{u}^2 + \overline{v}^2 + \overline{w}^2\right), \qquad [27]$$

where m is the mass of the liquid in motion, can be computed from

$$\sigma_{\overline{\mathrm{K}}} = m\sqrt{\frac{1}{n}\left(\overline{u}^2\sigma_u^2 + \overline{v}^2\sigma_v^2 + \overline{w}^2\sigma_w^2\right)}. \qquad [28]$$

The fluctuating components of the velocity vector are calculated by using Reynolds decomposition. The u' fluctuating component of the instantaneous velocity can be obtained from

$$u' = u - \overline{u}\,. \qquad [29]$$

The error for the fluctuating components of the velocity can be calculated from

$$\sigma_{u'} = \sqrt{\sigma_u^2 + \sigma_{\overline{u}}^2} = \sqrt{\frac{n+1}{n}}\,\sigma_u, \qquad [30]$$

and similarly for the other fluctuating components. Finally, the turbulent kinetic energy,

$$k = \frac{1}{2} m\left(u'^2 + v'^2 + w'^2\right), \qquad [31]$$

has an error associated given by

$$\sigma_k = m\sqrt{\frac{n+1}{n}\left(u'^2\sigma_u^2 + v'^2\sigma_v^2 + w'^2\sigma_w^2\right)}. \qquad [32]$$

5.2. Theoretical background

Newton's second law of motion states that the product of the mass and the acceleration experienced by a body equals the total external force acting on the body, that is

$$m\frac{D\mathbf{u}}{Dt}=\mathbf{F}, \qquad [33]$$

where **F** is the sum of all external forces, and

$$\frac{D}{Dt}=\frac{\partial}{\partial t}+\mathbf{u}\bullet\nabla \qquad [34]$$

is the substantial, or substantive, acceleration. This is the acceleration following the body (the Lagrangian approach), and contains a local contribution, for unsteady flow, and a contribution due to the convection of the flow.

Consider now a fluid element, and apply [33] to it. Then, when the fluid element is in motion two kinds of external forces act on it. One is a gravitational force, which acts throughout the mass of the fluid element. The other force acts on the fluid element surface. This force is composed of the pressure and friction forces. If the fluid is incompressible and Newtonian with density, ρ, and viscosity, μ, being constant, and the components of **F** are considered, [33] can be written as

$$\rho\frac{D\mathbf{u}}{Dt}=\rho\mathbf{g}-\nabla p+\mu\nabla^2\mathbf{u}, \qquad [35]$$

which are known as the Navier-Stokes equations (NSE).

The continuity equation for an incompressible flow,

$$\nabla\bullet\mathbf{u}=0, \qquad [36]$$

and the NSE, [35], are sufficient to solve for the unknowns **u** and p, provided appropriate boundary conditions are applied.

For a system with two phases, one of them being continuous and the other dispersed, the continuity and the NSE need to be solved for both phases. Interfacial relationships are then required to close the problem. Consider a solid particle in a flow stream. The requirement of no flow through the particle's surface implies that the normal and tangential flow velocities are zero relative to the solid particle velocity. The tangential velocity condition is known as the *non-slip*

condition, while the normal velocity condition is known as the *kinematic* condition.

The difference between fluid and solid particles cannot be neglected in the calculations of the velocity field. In a viscous fluid particle there exists an internal velocity field, or internal circulation, and the velocity at different locations on the particle can be different, for example there might be a velocity difference at the center and the surface of the fluid particle. For a fluid particle in a continuous fluid, additional boundary conditions are required to completely close the continuity and NSE for each phase. These additional boundary conditions are that the normal and tangential stresses must be balanced at the interface. These balances of stresses reflect the Newton's third law of motion. The stress is a consequence of the pressure field around the particle, and the tangential stress is due to shearing on the surface of the fluid particle.

By taking the curl of [34], the vorticity transport equation can be obtained as

$$\frac{D\boldsymbol{\omega}}{Dt}=\frac{\partial\boldsymbol{\omega}}{\partial t}+\mathbf{u}\bullet\nabla\boldsymbol{\omega}=\boldsymbol{\omega}\bullet\nabla\mathbf{u}+\nu\nabla^2\boldsymbol{\omega}. \qquad [37]$$

This equation states that the change in local vorticity plus the convection of vorticity by the flow equal the stretching or compression of the vorticity by the flow plus a diffusion term due to viscous friction. This equation is frequently used to describe the circulatory motion inside the wake of a bluff body. The wake is the region downstream a body in a flow, where there exists vorticity. The rotational flow inside a wake is due to the magnitude difference of the pressure and velocity between the outer and interior regions of the wake. For two-dimensional axisymmetric flows, the first term on the right hand side of [37] is equal to zero, which, in such a case, means that the distribution of vorticity is due only to viscous diffusion.

Analytic solutions for the flow around rigid and fluid particles of spherical shape are only available for Re < 1 (Re = $\rho\, U\, d\, /\, \mu$, where U is the free stream velocity and d the particle's diameter). For intermediate Re, numerical solutions exist, but usually limited to steady and axisymmetric flows. In these studies, the most common approach is to use the potential flow theory, limiting the boundary layer to a very small area surrounding the spherical particle. The boundary layer theory has been applied with success only for high Re (Re > 3000). For lower Re, the main difficulties are that the predicted velocity and pressure distributions are comparable to the experimental data up to 20 to 30 degrees from the front stagnation point on the particle's surface (Clif *et al.* 1978).

The study of the turbulence structure in a two-phase bubbly flow is one of the problems in which experimental, numerical and theoretical work is being extensively done nowadays. It is now considered that the turbulence in two-phase flow has two different sources: one is the turbulence generated in the continuous liquid phase, and the other is the turbulence induced by the movement of the bubbles in the flow. This last agitation due to the bubbles has been called pseudo-turbulence (Lance & Bataille 1991).

Most of the difficulties faced by the experimental and numerical communities when studying turbulence structure are the large range of time and length scales existing in turbulent flows. Consider, for example, the case of a single bubble rising in water. In this case all the liquid turbulence is pseudo-turbulence. The ratio of the velocity magnitude for positions close to the bubble to the points several bubble diameters away from the bubble's surface is orders of magnitude. This implies stiff differences in the time and length scales along at such given positions. Further, the wake of the bubble causes flow fluctuations that reache up several bubble diameters.

The most common approach to describe the flow field around a rising bubble is the potential flow. For dispersed bubbly flow, the influence of each bubble on the liquid motion is applied by using the superposition principle. Potential flow fails in describing the flow in the wake of the bubble, so it is clear that the superpositioning effects will not provide an accurate prediction of a bubbly flow.

The Reynolds stress tensor transport equation for a two-phase system can be written as:

$$\frac{D}{Dt}\left(\overline{\mathbf{u}'\mathbf{u}'}\right) = \mathrm{Diff}\left(\overline{\mathbf{u}'\mathbf{u}'}\right) + \mathbf{P} + \Phi - \varepsilon + \Pi\,, \qquad [38]$$

where the left hand side of the equation represents the convection of the stress components by the mean flow. On the right hand side presents the diffusion term, Diff; the production, **P**, due to liquid shear; the distribution of the stresses, Φ, due to pressure fluctuations; the dissipation term, ε; and an interfacial term, Π; respectively. This equation takes into account the liquid turbulence in the two-phase flow momentum equations. It is assumed that the stress tensor is composed of the single-phase liquid turbulence, denoted here by *(l)*, and the bubble's pseudo-turbulence, denoted by *(b)*. Consequently, it can be written as: